

A high temperature W₂B cermet for compact neutron shielding

Michail Athanasakis^a, Eugene Ivanov^b, Eduardo del Rio^b, Samuel A. Humphry-Baker^{a,*}

^a*Department of Materials, Imperial College London, London SW7 2BP, UK*

^b*Tosoh SMD Inc. 3600 Gantz Rd., Grove City, OH 43123, USA*

Abstract

We have developed a new material for neutron shielding applications where space is restricted. W₂B is an excellent attenuator of neutrons and gamma-rays, due to the combined gamma attenuation of W and neutron absorption of B. However, its low fracture toughness (~ 3.5 MPa) and high melting point (2670 °C) prevent the fabrication of large fully-dense monolithic parts with adequate mechanical properties. Here we meet these challenges by combining W₂B with a minor fraction (43 vol.%) of metallic W. The material was produced by reaction sintering W and BN powders. The mechanical properties under flexural and compressive loading were determined up to 1900 °C. The presence of the ductile metallic W phase enabled a peak flexural strength of ~ 950 MPa at 1100 °C, which is a factor of 2-3 higher than typical monolithic transition-metal borides. Its ductile-brittle transition temperature of ~ 1000 °C is typical of W-based composites, which is surprising as the W phase was the minor constituent and did not appear to form a fully continuous network. Compression tests showed hardening below ~ 1500 °C and significant elongation of the phase domains, which suggest that by forging or rolling, further improvements in ductility may be possible.

Keywords: tungsten boride, flexural strength, DBTT, cermets, neutron shielding, fusion reactors

1. Introduction

Advanced shielding materials are needed in many nuclear shielding technologies where space is limited including isotope containers, collimators, beam stops, and compact nuclear fission and fusion reactors. Space limitation is a particular concern for compact reactors and the recently-validated spherical tokamak fusion reactor [1], which could offer dramatically reduced costs and faster prototype development compared to conventional reactors [2–4]. Shielding these reactors is challenging around the high-temperature superconductors (HTS) within the central column. The HTS tapes must be protected from irradiation-induced degradation and power deposition, leading to cryostat heating, which would otherwise reduce the tokamak lifetime and plant efficiency.

Tungsten (W) is often the default choice of advanced shield due to its excellent gamma and neutron attenuation. It is used extensively in fusion reactors due to its extremely high melting point, high thermal conductivity, low sputtering yield, and low tritium retention [5–8]. However, tungsten has a relatively low cross section for neutron capture, particularly at thermal neutron energies, hence new highly-attenuating materials are needed.

Recent calculations show that the most efficient shielding materials for compact fusion reactors could be tungsten boride ceramics [9–11]. Their outstanding performance can be explained on the basis that they combine the gamma-attenuation properties of W with the neutron absorbing characteristics of boron. This combination has been shown using Monte-Carlo N-Particle MCNP calculations to have superior neutron attenuation efficiency compared to pure W or other advanced

*Corresponding author: shumphry@ic.ac.uk

shields such as WC [9–11]. The overall reduction in power deposition of WB-based shields is sensitive to the tungsten-to-boron ratio, with WB showing improved reduction in power compared to WB_2 [10]. The comparative performance at lower boron contents, e.g. W_2B or below, remains unstudied.

Because of their high melting temperature, monolithic tungsten borides are challenging to fabricate as fully dense parts. There are five stable compounds observed experimentally: W_2B , WB, WB_2 , W_2B_5 , and WB_4 [12]. Two others, WB_3 and WB_5 , have also been predicted [13, 14]. Of the stable compounds, W_2B has the highest density (16.6 g/cc [15]) and is the most thermodynamically stable at high temperatures [12, 16]. Although boron is more easily diffused in tungsten than in other transition metals [17], it is still relatively slow [18], therefore the bulk fabrication of tungsten boride from constituent elemental powders requires high pressures and temperatures (typically 1700 °C–2100 °C [16]) and/or advanced powder-processing techniques such as spark plasma sintering [19], solid state reaction [18], self-propagating high-temperature synthesis [20], or high-energy ball-milling [21].

As well as being challenging to fabricate, tungsten borides are hard and brittle. The literature on their mechanical properties is almost exclusively focused on understanding and characterising their hardness [13, 14, 22–25], which increases with boron content, reaching ~ 40 GPa for WB_2 [26] and WB_4 [24]. High hardness in transition metal (TM) borides is due to short TM-TM and TM-B covalent bonds [22, 27, 28]. Ab initio calculations show that in W_2B the W-W bonds were shorter than in the pure metal [12]. Their superior hardness is also associated with brittleness [16, 19, 29, 30]. Their toughness is predicted to vary in the range of 3–4 MPa m^{1/2} depending on the boron content [31]. Although these predictions are yet to be experimentally validated, wear tests show that WB is at least more brittle than W [17].

Previous efforts to improve the properties of tungsten boride, beyond incremental improvements like porosity and grain size optimisation,

have focused on additions of ductile TM elements. Such approaches are limited however, due to boron’s high reactivity with such elements other than Sn, Zn, Cu, and Ag [32]. Thus, when powders are co-sintered they react to form brittle ternary intermetallic compounds, commonly WMB (ϕ -phase) or W_2MB_2 (ω -phase). Due to the brittleness of these compounds, either rapid sintering cycles are needed to mitigate the kinetics of the reaction (as has received some success in the case of B_4C -Al composites [33]) or excessive quantities of the metallic additions are needed in order to guarantee the retention of a ductile phase after the reaction. For example, in the case of ϕ -phase composites, as is seen in the W-Fe-B system [11], Fe contents of >33.3 at.% are required, which degrade the material’s neutron attenuation characteristics.

Here we develop a new approach for toughening tungsten boride without forming detrimental ternary borides by employing a small volume fraction of metallic W, forming a W_2B -W cermet. Currently there is little known about the W_2B -W system. It has been shown that small additions of W_2B (<0.67 at.%) can retard grain growth in metallic W [31]. Composites with higher boron contents (up to 65 at.%) have been fabricated [34], however they were highly porous and therefore the effect of B content on properties could not be reliably determined. Here we fabricate a fully-dense W_2B -W cermet with a W phase fraction of 43 vol.%. The presence of the W phase enables significantly higher ductility and strength compared to typical transition metal borides. Its high temperature mechanical properties are more typical of W-based composites, which is surprising as W is the minor volume fraction phase.

2. Materials and methods

2.1. Sample preparation

The W_2B -W specimen was produced at Tosoh SMD by hot pressing powders of W and BN in a graphite die above 1700 °C in vacuum. The ratio of W to BN powders was 97:3 wt.%, which corresponds to a nominal B content of ~ 1.27 wt.%. During sintering the boron nitride decomposed,

forming di-tungsten boride (W_2B) and nitrogen gas. Further details can be found in a previous study [35]. Electrical discharge machining (EDM) was used to cut samples for flexion and compression tests. After cutting, the flexural samples were milled with a high speed SiC disk so that the faces normal to the loading axis were parallel. Samples were then ground progressively with diamond-impregnated grinding disks with grit sizes of P80, P220, and P1200 (mean particle size of 200 μm , 68 μm , and 15 μm respectively) in order to remove damage from the EDM and milling steps. To prevent stress concentrations at the corners, the four edges across the length of each sample were beveled. Compression samples were ground to P220 only.

2.2. Mechanical testing

All tests were performed within an MRF, Inc. furnace equipped with graphite push rods, housed within an Instron universal tester. The load was recorded using an Instron 2527 Series Dynacell load cell with dynamic rating of 25 kN. The applied load was recorded with an uncertainty of 0.5%. A high-vacuum atmosphere ($<4.0 \times 10^{-4}$ torr) was maintained using a Varian Agilent DS102 rotary vacuum pump and a tungsten-filament ionisation gauge. The sample was heated at a constant rate of 20 $^{\circ}C/min$ and equilibrated at the set-point temperature for five minutes before each test. The temperature was recorded with two W-WRe thermocouples positioned adjacent to the sample.

Flexural strength was determined in the three-point bending (TPB) geometry on bars of $\sim 2 \times 3 \times 25$ mm with a load-span of 20 mm. Each test was performed at a nominal displacement rate of 0.5 mm/min, corresponding to a strain rate of $\sim 2 \times 10^{-4} s^{-1}$. Samples were deformed until the load dropped to 90% of the peak value, or until ~ 1 mm of deflection, whichever occurred first. In the brittle regime ($T < 1200$ $^{\circ}C$), at least three TPB tests were performed at each temperature. The engineering stress was determined using the formula [36]:

$$\sigma_f = \frac{3Fl}{2wh^2} \quad (1)$$

where F is the applied load, l is the support span, and w and h are the sample width and height (thickness) respectively. The flexural strength (σ_f^{max}) corresponded to the stress at maximum applied load, F_{max} .

Compression tests were performed on cuboidal samples of approximately $3 \times 3 \times 6$ mm and $2 \times 2 \times 4$ mm, for tests >1600 $^{\circ}C$ and <1600 $^{\circ}C$, respectively. Samples were compressed by cylindrical graphite push rods. To protect the rods from indentation by the sample, each sample was sandwiched by 3 mm-thick SiC spacers. The yield strength was calculated using the 0.2% strain offset method. All tests were performed with a nominal strain rate of $10^{-3} s^{-1}$ and terminated when the load exceeded 5 kN. Elastic deflection of the sample and machine was accounted for by subtracting a linear fit to the elastic regime of the load-deflection curve.

2.3. Characterisation

The as-received material was characterised by X-ray diffraction (XRD) using a Panalytical X'Pert powder diffractometer using a Cu source operated at 40 kV and 40 mA. Patterns were collected at scan rate of 2° per minute from $20-90^{\circ} 2\theta$. For determination of the lattice parameters, systematic errors in peak position were corrected for using the Nelson-Riley method. Cross-sectional micrographs were collected using a Zeiss Sigma 300 Field Emission Gun Scanning Electron Microscope (SEM) operated in Secondary Electron Imaging (SEI) mode with the sample tilted to 25° to improve Z-contrast. Phase fractions were determined using point counting stereology on an array of >200 points. Pore size and volume fraction were determined by manually tracing ~ 180 pores and determining their area using Image-J. Fracture surfaces were imaged using a JSM 6010 SEM operated in SEI mode.

3. Results

3.1. As-received material

The XRD scan in Fig. 1 shows that the only phases formed after hot-pressing were bcc-W and tetragonal W_2B . The lack of any BN peaks shows

that it fully reacted with the W via the reaction $BN + 2W \rightarrow W_2B + 0.5N_2(g)$. The lattice parameter for W was $a = 0.317$ nm and for W_2B were $a = 0.558$ nm; $c = 0.475$ nm. These values are within 0.001 nm of the crystallographic database values, which are $a = 0.316$ nm (code 001-1203) and $a = 0.557$ nm; $c = 0.474$ nm (025-0990) respectively.

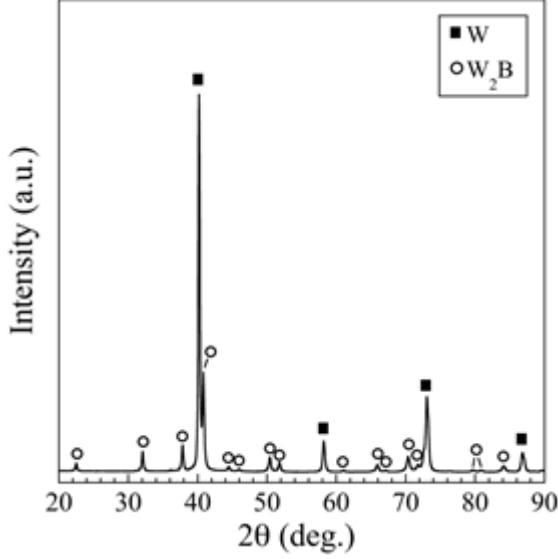


Figure 1: XRD spectrum of as-received material showing W_2B and W as the only phases present.

In the SEM micrograph shown in Fig. 2(a), the dark phase corresponds to W and the light phase to W_2B (the sample has been tilted to increase contrast). W_2B forms an interconnected network that occupies the major volume fraction of 57%. The volume fraction of the W phase is 43% and is arranged as loosely-connected particles of 5-50 μm in diameter. The particles are themselves composed of grains of ~ 5 μm in diameter. The 57 vol.% W_2B phase is slightly lower than that predicted from the 1.27 wt.% boron added, which corresponds to 61 vol.% W_2B . This suggests that some boron is dissolved into the W phase or that the stoichiometry of the W_2B is slightly boron-rich. The high-resolution micrograph shown in Fig. 2(b) shows the grain structure and porosity more clearly. There is no phase-contrast from lack of sample tilting. W regions appear depressed as they are more easily polished than W_2B regions. The pores are 1-2 μm in diameter. Stereology

measurements show they occupy a volume fraction of $\sim 1.1\%$.

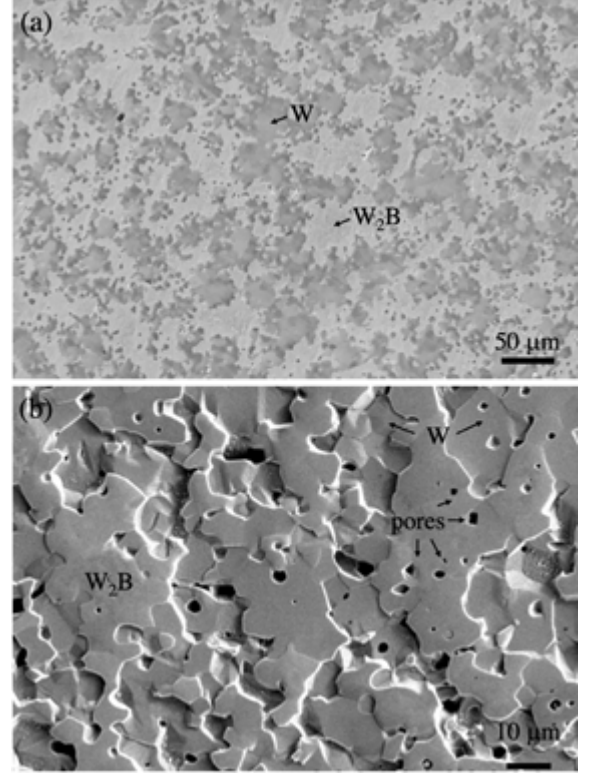


Figure 2: (a) SEM micrograph of as-received material with sample tilted. W is the dark phase and W_2B is the light phase. (b) High-resolution micrograph showing pores of 1-2 μm and volume fraction of $\sim 1.1\%$.

3.2. Three-point bending

Fig. 3(a) shows some typical stress-displacement curves during three-point bending (TPB). All curves show a linear elastic region up to a deflection of ~ 0.1 mm. After that, the curves deviate significantly. Up to 1000 $^{\circ}\text{C}$, the samples are brittle; the specimens fracture immediately after yielding at a stress of ~ 700 MPa. Between 1000 and 1200 $^{\circ}\text{C}$, there is some plastic deflection, which increases with temperature from ~ 0.05 mm at 1000 $^{\circ}\text{C}$, to ~ 0.7 mm at 1200 $^{\circ}\text{C}$. Fig. 3(b) shows the flexural strength values extracted from part (a) as a function of temperature. The figure confirms that the flexural strength between 500 and 1000 $^{\circ}\text{C}$ is approximately constant at ~ 700 MPa. The flexural strength then peaks around 1100 $^{\circ}\text{C}$ at 954 ± 27 MPa at 1100 $^{\circ}\text{C}$.

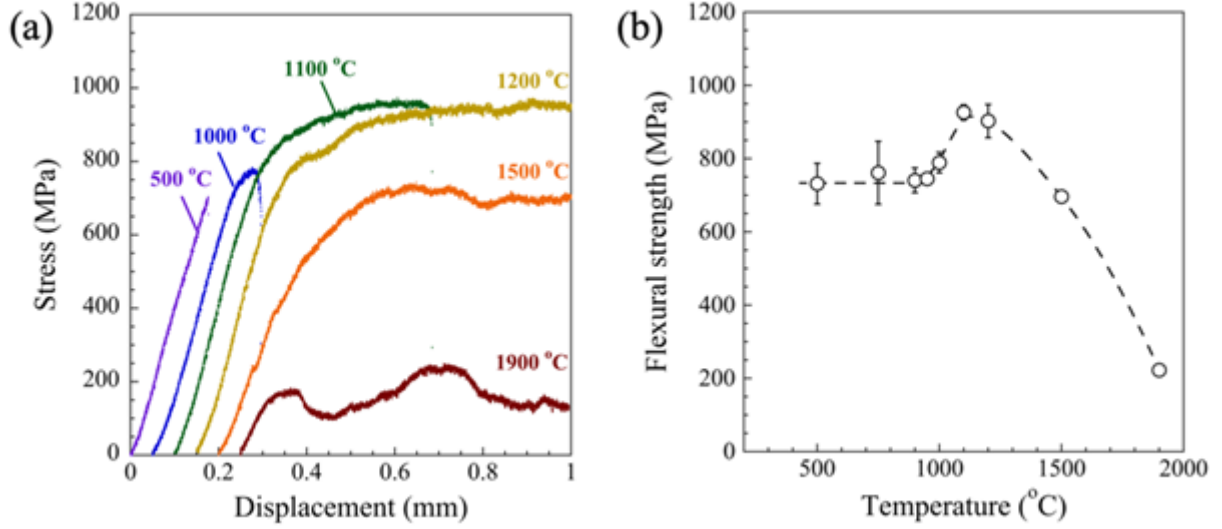


Figure 3: (a) Typical stress-displacement curves at various temperatures. Curves have been offset by displacement increments of 0.05 mm for clarity. (b) Corresponding flexural strength. Error bars indicate standard deviation in 3 tests.

Above 1200 °C, the flexural strength begins to decrease rapidly.

Fig. 4(a) shows the ductile-to-brittle transition by plotting the average specimen deflection vs. temperature. Below 900 °C, a small deflection of ~ 0.1 mm is observed, mostly due to elastic deformation of the test rig. Above 1200 °C, a large deflection of ~ 1 mm or more is recorded due to extensive plastic deformation of the specimen. To determine the transition temperature, the data has been fitted with the expression [37]:

$$\delta = \delta_{br} + \frac{\delta_{pl}}{1 + \exp\left(-\frac{T - T_{DBT}}{\Delta T}\right)} \quad (2)$$

where δ_{br} is the deflection at the lower shelf, i.e. elastic deformation only, δ_{pl} is the increment of plastic deflection in the sample, T is the temperature, T_{DBT} is the ductile-brittle transition temperature, and ΔT is the width of the transition. The fit shows a T_{DBT} of 1065 °C. Visually, this transition can be seen in the post-test sample photograph in Fig. 5(b). The samples tested at 900 °C and below broke clean in two, while the samples tested at 1000 and 1100 °C showed large cracks on the tensile face, which did not propagate throughout the entire thickness. Samples tested at 1200 °C and above showed no large cracks. The degree of plastic deformation clearly increases with temperature.

The ductile-brittle transition is seen on the tensile surfaces of the bend specimens in Fig. 5. Part (a) shows the cracked-surfaces immediately below the DBTT, at 1000 °C, while part (b) shows them immediately above it at 1100 °C. In both samples there is a large primary crack in the centre of the sample, which did not propagate through the specimen thickness. In the 1000 °C sample, there are a few additional microcracks formed in the vicinity of the primary crack, all within ~ 50 μm of it. However, in the 1100 °C sample, there is a significant increase in the number of such microcracks and the width over which they spread increases to 1-2 mm. Similar microcracks surrounding the primary crack were observed in samples tested at 1200 °C, indicating such microcracking is associating with an increasingly ductile mode of failure.

The role of each phase in the ductile-brittle transition is shown in Fig. 6. Fracture surfaces of the specimens are shown after testing in the brittle regime at (a) 500, (b) 750, (c) 1000 °C and in the ductile regime at (d) 1200 °C. The surfaces show increasingly ductile behavior with increasing temperature. In (a), there is a mixture of intergranular fracture in the W phase (labelled *W-ig*), as indicated by the faceted surfaces, and transgranular fracture in the W_2B phase (labelled *W₂B-tg*), as indicated by the smooth surface. In

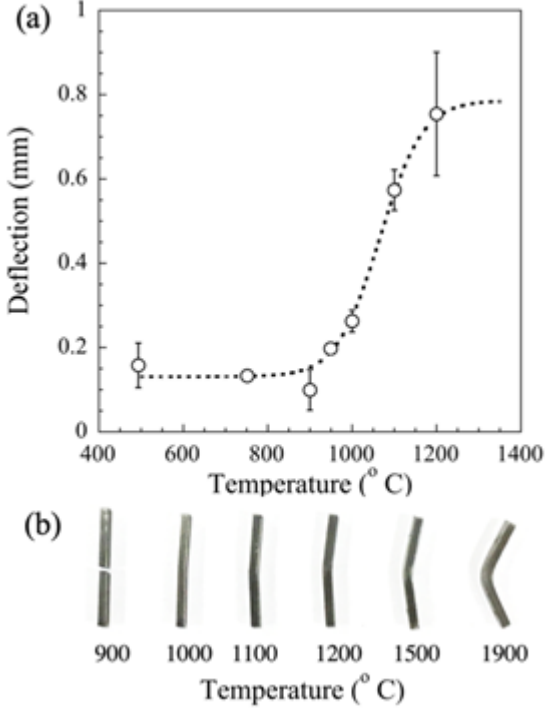


Figure 4: (a) Maximum deflection before fracture of bend specimens. Error bars correspond to one standard deviation between 3 samples. (b) Photograph of typical samples after testing.

(b), a portion of the intergranular fracture in the W is replaced by a small area of dimples or microcavities, indicated as *W-mc*. In (c) the portion of intergranular fracture decreases furthermore, while in (d) no intergranular fracture is observed at all in W, being replaced entirely by microcavity formation. By contrast, the W_2B phase appears to fracture in a brittle manner at all temperatures.

3.3. Compression

Fig. 7(a) shows the nominal stress-strain curves under compression at 1100-1900 °C. All curves show an approximately linear elastic regime up to a stress of 200-600 MPa. The strain hardening behavior is strongly temperature-dependent. In the region 1700-1900 °C, the slope was relatively flat, which indicates perfectly plastic flow, suggesting that dislocations are annihilated as they form. At 1500 °C and below the slopes become more positive, indicating that significant work hardening occurred. The degree of work hardening is characterised in more detail in part (b) along with values for the yield strength. The yield strength,

plotted on the primary y-axis, shows a monotonic decrease with temperature, the degree of which accelerates above ~ 1500 °C. Similarly, the strain hardening coefficient, n , calculated by fitting the post-yield curve with an expression of the form $\sigma = A\epsilon^n$, plotted on the secondary y-axis, shows a transition from a value of about $n = 0.2$ below 1500 °C to about $n = 0.05$ above it, coinciding with the onset of perfect plastic flow.

Fig. 8 shows an SEM micrograph of the sample compressed at 1800 °C to a nominal strain of 0.56, with the micrograph's vertical axis oriented parallel to the compression axis, as shown in the schematic. The dark phase corresponds to W and the lighter phase corresponds to W_2B . Compared to the SEM micrograph of the as-received material shown in Fig. 2(b), the W phase domains are significantly elongated. The length of the domains is ~ 100 μm , and their width is ~ 20 μm . Elongation was also seen at lower testing temperatures. The elongation axis of the phase domains is not perfectly perpendicular to the compression axis, which could be due to slight sample misalignment or friction between the sample and platens.

4. Discussion

4.1. Toughening from W-phase

The most surprising aspect of this study was the comparatively high flexural strength of W_2B -W composites compared to monolithic boride ceramics. Fig. 9 shows the high temperature flexural strength of W_2B -W compared to literature studies on monolithic transition metal boride compounds: ZrB_2 [38], NbB_2 [39], HfB_2 [40], and TiB_2 [41]. The difference in strength in the temperature range 400-1200 °C is significant. The strength of the transition metal borides are typically 200-400 MPa, while W_2B composite studied here is 700-1000 MPa. The shape of the curves is also different; the monolithic borides decrease in strength monotonically or remain fairly constant, while the W_2B composite increases in strength up to 1200 °C. This strength increase was shown to coincide with the onset of significant ductility in Fig. 4, which was accompanied by the formation of microcavities in the W regions shown

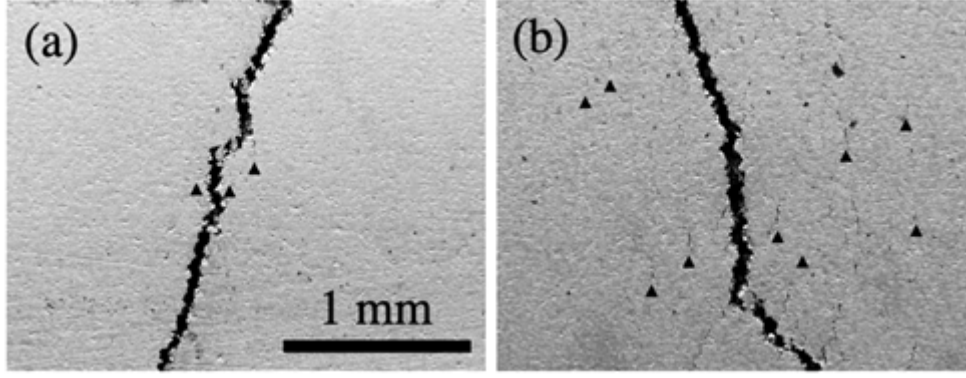


Figure 5: SEM micrograph along the axis of maximum tension of fractured W_2B-W after TPB. (a) 1000 and (b) 1100 °C. Microcracks are indicated by triangles.

in Fig. 6. It is also worth pointing out that the monolithic ceramic studied in [38–41] did not observe transition to ductile behavior at high temperature. It is therefore reasonable to conclude that the enhanced strength and ductility of W_2B-W over monolithic borides is caused by the presence of the W.

Fig. 9 also shows that the strength advantage of the W_2B-W composite over monolithic borides is lost by between 1500 and 1900 °C. The reason for the rapid softening of W_2B-W over monolithic borides is lost between 1500 and 1900 °C. The reason for the rapid softening of W_2B-W in this temperature range is again likely due to the W phase rather than the boride. Although the strength of W has not been characterised at this temperature, Pisarenko et al. showed that the hardness of W fell to only 200 MPa at ~ 1900 °C [48], corresponding to a compressive strength of ~ 70 MPa, which is well below the strength of typical borides. This latter point is addressed in the following section.

4.2. Ceramic volume fraction

Although tungsten was not the major constituent in the present study, a comparison of W-based composites is pertinent on the basis that such materials typically observe a DBTT ~ 1000 °C in the recrystallized state [43], as was the case here. We therefore briefly discuss their typical properties. The flexural strength of pure tungsten at room temperature via TPB is ~ 800 MPa [13, 14]. At elevated temperatures it continually decreases, e.g. to 680 MPa at 600 °C [45],

which is lower than the present study.

By dispersing ceramic particles within a tungsten matrix, strengths comparable to W_2B-W have been achieved. Table 1 summarises the literature on the flexural strength of ceramic particle-dispersed tungsten. It is important to note that such studies report ceramic volume fractions of 3-30 vol.%, which are substantially lower than the present study (57 vol.%). Lower strengths are reported for oxide-dispersed W, such as Y_2O_3 and La_2O_3 [43, 44], which lie in the range 420-855 MPa. However, comparatively higher peak strengths are reported for carbide-dispersed W, such as ZrC and TiC, which are often between 1050-1152 MPa, and the highest peak strength was reported for ZrB_2 -dispersed W at 1279 MPa [47]. The reason for the lower strength in the present study is likely the higher content of ceramic phase, which led to some porosity, as shown in Fig. 2(b). This view is supported by systematic studies on the effect of TiC volume fraction, which show that strength peaks at 30 vol.-% [49], due to excessive porosity in more highly reinforced materials.

The temperature at which the peak stress is observed (T_{max}) in W_2B-W is higher than in any previous studies shown in Table 1. There appears to be a positive correlation between T_{max} and ceramic phase volume fraction. Metal carbide additions with fractions of 20-30% e.g. W-ZrC [45, 46], and W-TiC [44, 49] tend to show peak strengths at $\sim 800-1000$ °C while smaller metal oxide fractions of 3-6%. e.g. W- La_2O_3 [44, 50], W- Y_2O_3

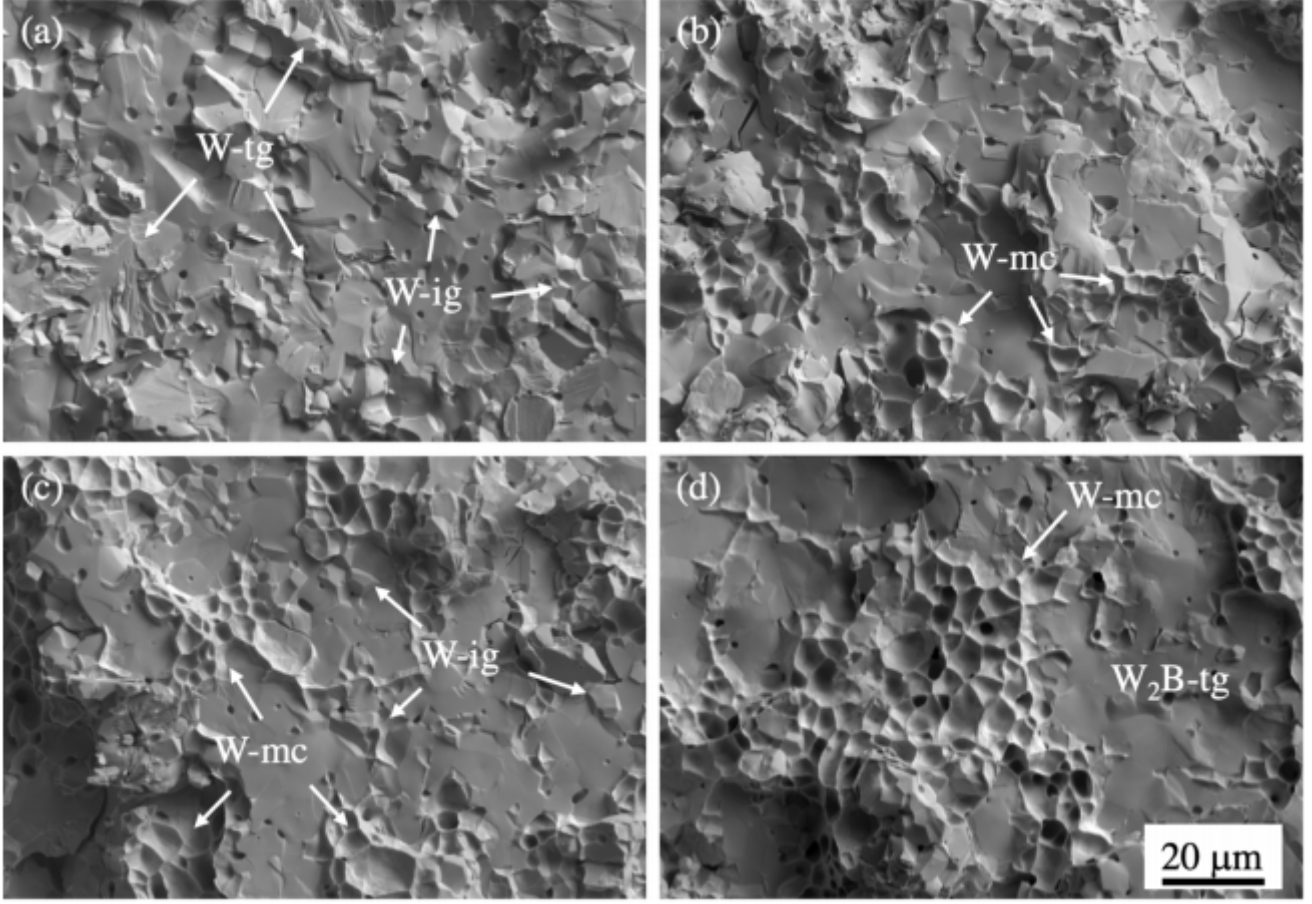


Figure 6: SEM micrographs of fractured bend specimens. (a) 500, (b) 750, (c) 1000, and (d) 1200 °C. In the W phase, a transition from transgranular (tg) to microcavity formation (mc) is seen between 750 and 1200 °C.

Table 1: Particle-reinforced tungsten composites and the resulting maximum flexural strengths. Compositions denoted by an asterisk have been converted from wt.-% to vol.-% using density values from Ref. [42].

Composition (vol. %)	Sintering method	Grain size (μm)	Max. strength (MPa)	Temperature at max. strength ($^{\circ}\text{C}$)	Reference
W	MA + HIP	12	170	600	Palacios et al. [43]
W	VHP	2	780	RT	Chen et al. [44]
W	VHP	3.5	800	RT	Song et al. [45]
W-3.5Y ₂ O ₃ *	MA + HIP	5.3 & 0.42 (bimodal)	420	600	Palacios et al. [43]
W-16.6TiC-2.5La ₂ O ₃ *	VHP	0.5	901	RT	Chen et al. [44]
W-5.8La ₂ O ₃ *	VHP	0.5	855	RT	Chen et al. [44]
W-20ZrC	MA	3.5	1052	800	Song et al. [46]
W-30TiC	VHP	3.5 & 2.5 (bimodal)	1150	1000	Song et al. [45]
W-3ZrB ₂ *	SPS	0.65	1279	RT	Wang and Yan [47]
W-57W ₂ B	VHP	5	954	1100	This study

[43, 51, 52] show peak strength at $\sim 25\text{-}600$ °C. In monolithic W the strength decreases monotonically with temperature [49]. The positive correlation between T_{max} and ceramic volume fraction is likely due to the inhibition of dislocation motion at high temperatures. It is therefore likely that the slightly higher peak-strength temperature reported in this study compared to previous works

is due to the higher volume fraction of ceramic phase.

4.3. Hardening by W₂B

The hardening role of the W₂B phase can be assessed by comparing the compressive strength of W₂B-W to pure W. Fig. 10 compares the yield strengths from Fig. 7 to the indentation hardness

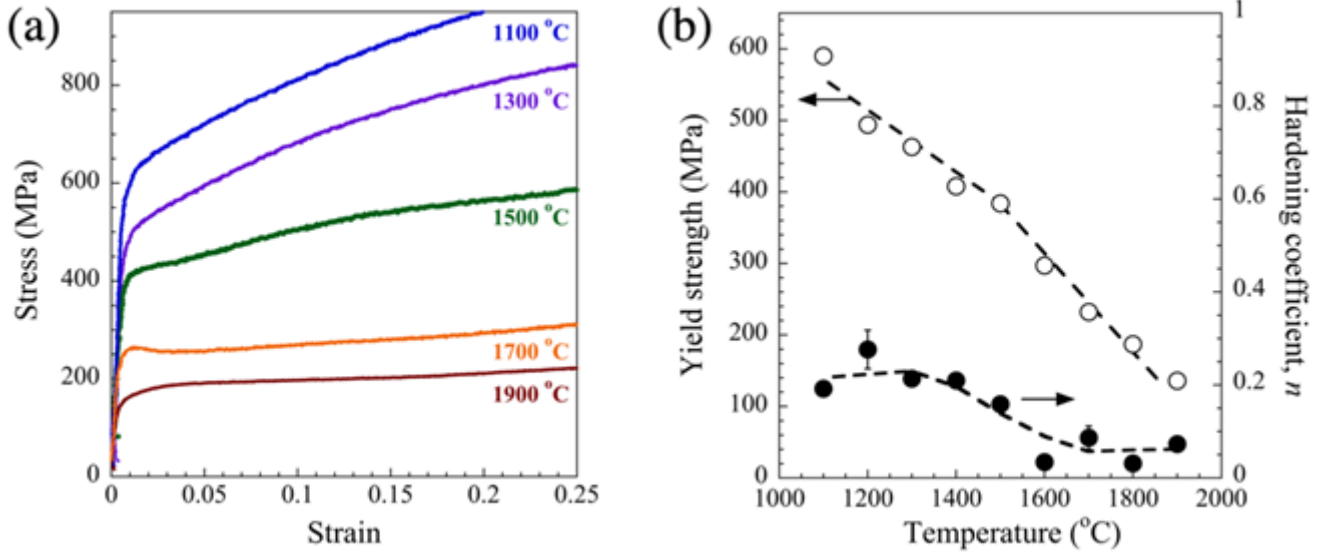


Figure 7: (a) Nominal stress-strain curves under compression. (b) Yield strength and strain hardening coefficient. Error bars represent deviation when only the first half of the data-set is used for fitting.

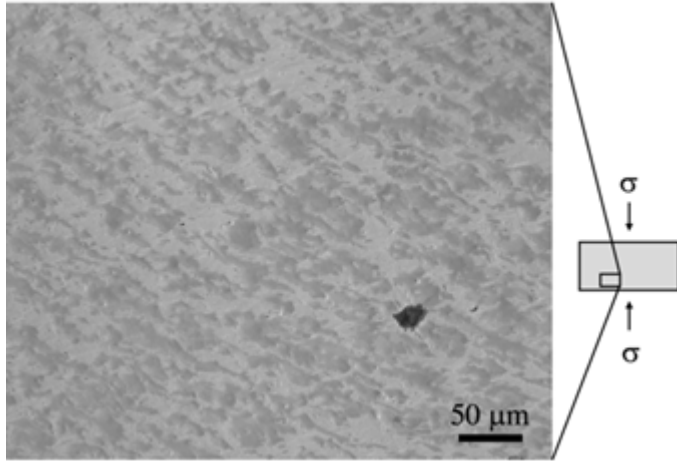


Figure 8: BSE-SEM micrograph of W_2B-W after compression at 1800 °C. Micrograph vertical axis is parallel to the compression axis.

data collected by Atkins and Tabor [53] and Pisarenko et. al [48]. The plot assumes that the hardness of W is 3 times its yield strength. On the basis of this assumption, the compressive strength of W_2B-W is $\sim 50\%$ higher than cold-worked W and perhaps a factor of 3 or so higher than annealed W. Thus, the flow stress in W_2B is expected to be at least 2-3 times higher than annealed W at these temperatures. This is in agreement with hardness predictions of W_2B at room temperature which report 12.7 GPa [14], i.e. a

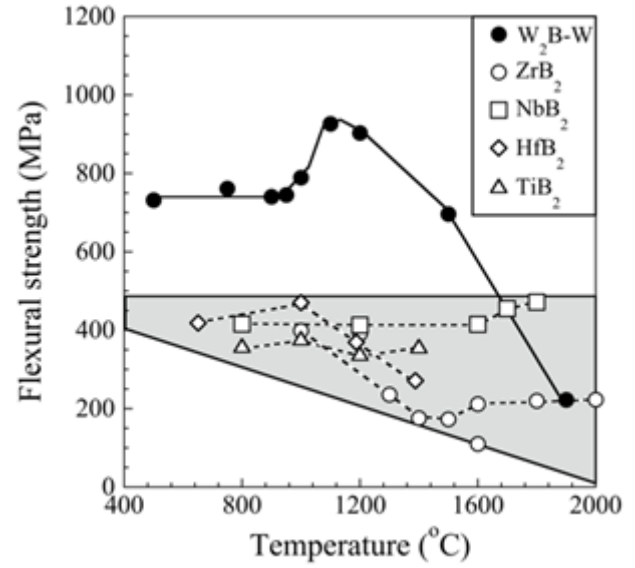


Figure 9: High-temperature flexural strength of W_2B-W compared to ZrB_2 [38], NbB_2 [39], HfB_2 [40] and TiB_2 [41].

factor of 4 higher than pure W (3.4 GPa [45]).

Fig. 10 may also give some evidence as to the transition from work hardening to perfect plastic flow in W_2B-W . Looking more closely at the data by Pisarenko et. al [48] it is clear that the hardness of the cold-worked and recrystallised tungsten converge between 1400 and 1600 °C, indicating that the dislocation networks generated dur-

ing cold-working become mostly annihilated at some point in this range. Since this is the same temperature range over which W_2B -W transitions from work hardening to perfect plastic (according to Fig. 7(b)), it can be concluded that this transition in W_2B -W is related to rates of defect-recovery in the W phase.

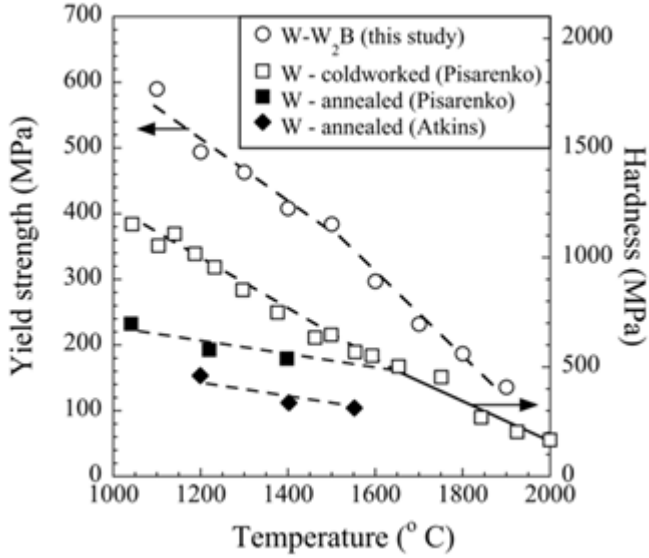


Figure 10: Compressive yield strength of W_2B -W (primary y-axis) compared to $1/3$ hardness of W (secondary y-axis). The W hardness data originally appears in Fig. 11 of Ref. [53] and Fig. 1 of Ref. [48].

4.4. Ductilisation by thermomechanical processing

The observations of elongation in phase domains in compressed W_2B -W (Fig. 8) suggests that thermomechanical processing (e.g. rolling, forging, swaging or extrusion) may enable improvements in toughness, following previous studies in tungsten-based materials. Strategies for tungsten ductilisation have been reviewed [54, 55]. Both studies agree that two strategies reliably reduce the DBTT of tungsten: 1) alloying with rhenium, which facilitates transgranular fracture [56] and the mobility of $1/2 < 111 >$ screw dislocations in W [57, 58], and 2) thermomechanical processing (TMP). The second ductilisation strategy, TMP, is an unusual route towards improved toughness. Contrary to the behavior of most

deformation-processed metals, where work hardening reduces ductility, TMP can decrease tungsten's brittleness [59–66]. The proposed mechanisms of ductilisation after TMP [54, 66] are: 1) reducing porosity; 2) aiding the movement of dislocations across grain boundaries by introducing small-angle boundaries; 3) increasing the number of high-mobility mixed and edge dislocations; 4) increasing the tortuosity of the crack path by introducing grain boundary texture, and 5) reducing impurity concentrations along the grain boundaries by refining the grain size.

Fig. 7(b) suggests that mechanism 3 could be operative during forging at temperature < 1500 °C, since the material work hardened and thus significant dislocation production is expected. Furthermore Fig. 8 suggests that mechanism 4 may be possible, at least when loaded perpendicular to the forging direction, since a crack running through the elongated phase domains would likely have to deviate to favor the more brittle (boride) phase. More work is needed in order to establish the degree of porosity reduction (mechanism 1), and production of new grain boundaries (mechanisms 2 and 5).

Table 2 summarises the results of a number of studies on the DBTT of TMP-ductilised pure tungsten and particle-dispersed tungsten composites. The majority of the rolling/forging temperatures are in excess of 1200 °C. However it is clear that cold rolling is more effective for ductilisation, since the lowest DBTT in Table 2 reported by Ref. [62] and Ref. [67] are both recorded after cold rolling, presumably because of greater dislocation and low-angle grain boundary production due to slower defect-recovery rates. The relatively high yield strength and brittleness of W_2B in comparison to W may make cold rolling W_2B -W at high strains challenging. However, due to the ability of the material to work harden even at temperatures as high as 1500 °C, hot rolling may still be effective.

5. Conclusions

We have developed a W_2B -based composite with improved properties and manufacturability

Table 2: Summarised results on studies on the DBTT of thermomechanically processed tungsten and particle-dispersed tungsten composites. Adapted from Table 2 in [54].

Material	TMP treatment	T_{TMP} (°C)	Grain size (μm)	Testing method	DBTT (°C)	Reference
W	0.1 mm film	400	0.8	Tensile	RT	Wei and Kecskes [62]
W	0.1 mm film		0.5	Tensile	RT	Reiser et al. [67]
W	Rolled	<1200	1-4	Charpy	125	Reiser et al. [59]
W	Rolled	2100	5-50 bimodal	TPB	180-230	Krsjak et al. [68]
W	Rolled	1450-1650	100×400	Tensile	<280	Habainy et al. [69]
W	Rolled	1450-1650	140×330	Tensile	250-300	Shen et al. [61]
W	Rolled	1500	100	Charpy	577	Zhang et al. [70]
W-1wt%La ₂ O ₃	Rolled+swaged	1350-1600	40	Charpy	700	Yan et al. [63]
W	Forged	>1200	1-20	Charpy	800	Rieth et al. [71]
W-1wt%La ₂ O ₃	Forged	>1200	1-20	Charpy	950	Rieth et al. [71]
W-0.2wt%TiC	Forged+rolled	1200-1500	1.6	TPB	180	Kitsunai et al. [72]
W-0.5wt%TiC	Forged	>1200	0.44	TPB	210	Kitsunai et al. [72]

compared to monolithic boride ceramics. Flexural and compression tests were performed up to 1900 °C and the resulting fracture surfaces and microstructure characterised. The most surprising conclusion is that the material shows broadly similar mechanical properties compared to majority tungsten-based composites, which is unexpected as W was the minor phase. Detailed conclusions can be summarised as follows:

- The flexural strength was 2-3 times higher than monolithic transition metal borides, which is explained by the presence of metallic W.
- The flexural strength was similar to ceramic-dispersed tungsten composites with much lower volume fractions of 3-30%, although the temperature of peak strength, 1100 °C, was higher than typically found in these composites, usually 600-1000 °C. This discrepancy is likely due to the relatively high ceramic phase content in this study.
- The DBTT was ~ 1060 °C. Fracture in the brittle regime was mostly intergranular for W domains and transgranular for W₂B. In the ductile regime, W increasingly fractured by the coalescence of microcavities. This confirmed the toughening effect provided by W.
- The compressive strength was a factor of ~ 3 higher than annealed W due to the higher flow stress in W₂B.

- Compression tests revealed phase elongation and when deformed below 1500 °C, dislocation accumulation as well. Cumulatively, these microstructural changes suggest that rolling or forging may improve ductility.

A systematic investigation of the effects of W₂B content, porosity and grain size is needed. Further work on thermomechanically processed specimens is also required, including characterisation of texture and grain boundary production. The effects of irradiation on the above properties is also yet to be studied.

Data availability

The raw unpublished supporting data is available on request.

Acknowledgments

S. A. Humphry-Baker was financially supported by the Imperial College Research Fellowship.

References

- [1] A. Costley, J. Hugill, P. Buxton, On the power and size of tokamak fusion pilot plants and reactors, Nuclear Fusion 55 (3) (2015) 033001. doi:10.1088/0029-5515/55/3/033001.
- [2] D. Clery, The new shape of fusion, Science 348 (6237) (2015) 854 LP – 856. doi:10.1126/science.348.6237.854.

- [3] B. Sorbom, J. Ball, T. Palmer, F. Mangiarotti, J. Sierchio, P. Bonoli, C. Kasten, D. Sutherland, H. Barnard, C. Haakonsen, J. Goh, C. Sung, D. Whyte, ARC: A compact, high-field, fusion nuclear science facility and demonstration power plant with demountable magnets, *Fusion Engineering and Design* 100 (2015) 378–405. doi:10.1016/J.FUSENGDES.2015.07.008.
- [4] A. Sykes, A. Costley, C. Windsor, O. Asunta, G. Brittles, P. Buxton, V. Chuyanov, J. Connor, M. Gryaznevich, B. Huang, J. Hugill, A. Kukushkin, D. Kingham, A. Langtry, S. McNamara, J. Morgan, P. Noonan, J. Ross, V. Shevchenko, R. Slade, G. Smith, Compact fusion energy based on the spherical tokamak, *Nuclear Fusion* 58 (1) (2018) 016039. doi:10.1088/1741-4326/aa8c8d.
- [5] H. Bolt, V. Barabash, W. Krauss, J. Linke, R. Neu, S. Suzuki, N. Yoshida, ASDEX Upgrade Team, Materials for the plasma-facing components of fusion reactors, *Journal of Nuclear Materials* 329–333 (2004) 66–73. doi:10.1016/J.JNUCMAT.2004.04.005.
- [6] R. Neu, R. Dux, A. Kallenbach, T. Pütterich, M. Balden, J. Fuchs, A. Herrmann, C. Maggi, M. O'Mullane, R. Pugno, I. Radivojevic, V. Rohde, A. Sips, W. Suttrop, A. Whiteford, t. A. U. Team, Tungsten: an option for divertor and main chamber plasma facing components in future fusion devices, *Nuclear Fusion* 45 (3) (2005) 209–218. doi:10.1088/0029-5515/45/3/007.
- [7] M. Kaufmann, R. Neu, Tungsten as first wall material in fusion devices, *Fusion Engineering and Design* 82 (5–14) (2007) 521–527. doi:10.1016/J.FUSENGDES.2007.03.045.
- [8] V. Philipps, Tungsten as material for plasma-facing components in fusion devices, *Journal of Nuclear Materials* 415 (1) (2011) S2–S9. doi:10.1016/J.JNUCMAT.2011.01.110.
- [9] C. Windsor, J. Morgan, P. Buxton, Heat deposition into the superconducting central column of a spherical tokamak fusion plant, *Nuclear Fusion* 55 (2) (2015) 023014. doi:10.1088/0029-5515/55/2/023014.
- [10] C. Windsor, J. Morgan, P. Buxton, A. Costley, G. Smith, A. Sykes, Modelling the power deposition into a spherical tokamak fusion power plant, *Nuclear Fusion* 57 (3) (2017) 036001. doi:10.1088/1741-4326/57/3/036001.
- [11] C. Windsor, J. Marshall, J. Morgan, J. Fair, G. Smith, A. Rajczyk-Wryk, J. Tarragó, Design of cemented tungsten carbide and boride-containing shields for a fusion power plant, *Nuclear Fusion* 58 (7) (2018) 076014. doi:10.1088/1741-4326/aabdb0.
- [12] E. Zhao, J. Meng, Y. Ma, Z. Wu, Phase stability and mechanical properties of tungsten borides from first principles calculations, *Physical Chemistry Chemical Physics* (2010). doi:10.1039/c004122j.
- [13] S. Q. Feng, F. Guo, J. Y. Li, Y. Q. Wang, L. M. Zhang, X. L. Cheng, Theoretical investigations of physical stability, electronic properties and hardness of transition-metal tungsten borides WB_x (x = 2.5, 3), *Chemical Physics Letters* 635 (2015) 205–209. doi:10.1016/j.cplett.2015.06.080.
- [14] A. G. Kvashnin, H. A. Zakaryan, C. Zhao, Y. Duan, Y. A. Kvashnina, C. Xie, H. Dong, A. R. Oganov, New Tungsten Borides, Their Stability and Outstanding Mechanical Properties, *Journal of Physical Chemistry Letters* 9 (12) (2018) 3470–3477. doi:10.1021/acs.jpclett.8b01262.
- [15] K. Persson, Materials Data on BW2 (SG:140) by Materials Project (2015). doi:10.17188/1187585.
- [16] L. Brewer, D. L. Sawyer, D. H. Templeton, C. H. Dauben, A Study of the Refractory Borides, *Journal of the American Ceramic Society* 34 (6) (1951) 173–179. doi:10.1111/j.1151-2916.1951.tb11631.x.
- [17] M. Usta, I. Ozbek, C. Bindal, A. H. Ucisik, S. Ingole, H. Liang, A comparative study of borided pure niobium, tungsten and chromium, *Vacuum* 80 (11–12) (2006) 1321–1325. doi:10.1016/j.vacuum.2006.01.036.
- [18] H. Itoh, T. Matsudaira, S. Naka, H. Hamamoto, M. Obayashi, Formation process of tungsten borides by solid state reaction between tungsten and amorphous boron, *Journal of Materials Science* 22 (8) (1987) 2811–2815. doi:10.1007/BF01086475.
- [19] K. A. Khor, L. G. Yu, G. Sundararajan, Formation of hard tungsten boride layer by spark plasma sintering boriding, *Thin Solid Films* (2005). doi:10.1016/j.tsf.2004.07.004.
- [20] S. Yazici, B. Derin, Production of tungsten boride from CaWO₄ by self-propagating high-temperature synthesis followed by HCl leaching, *International Journal of Refractory Metals and Hard Materials* 29 (1) (2011) 90–95. doi:10.1016/j.ijrmhm.2010.08.005.
- [21] M. Stubičar, A. Tonejc, N. Stubičar, X-ray diffraction study of F W-B elemental powder mixtures after high-energy ball-milling, *Fizika A* 4 (1) (1995) 65–72.
- [22] R. B. Kaner, J. J. Gilman, S. H. Tolbert, Designing superhard materials (5 2005). doi:10.1126/science.1109830.
- [23] R. Mohammadi, A. T. Lech, M. Xie, B. E. Weaver, M. T. Yeung, S. H. Tolbert, R. B. Kaner, Tungsten tetraboride, an inexpensive superhard material, *Proceedings of the National Academy of Sciences of the United States of America* 108 (27) (2011) 10958–10962. doi:10.1073/pnas.1102636108.
- [24] A. T. Lech, C. L. Turner, R. Mohammadi, S. H. Tolbert, R. B. Kaner, Structure of superhard tungsten tetraboride: A missing link between MB2 and MB12 higher borides, *Proceedings of the National Academy of Sciences of the United States of America* 112 (11) (2015) 3223–3228. doi:10.1073/pnas.1415018112.

- [25] Y. Chen, D. He, J. Qin, Z. Kou, Y. Bi, Ultrasonic and hardness measurements for ultrahigh pressure prepared WB ceramics, *International Journal of Refractory Metals and Hard Materials* 29 (2) (2011) 329–331. doi:10.1016/j.ijrmhm.2010.12.006.
- [26] R. Hahn, V. Moraes, A. Limbeck, P. Polcik, P. H. Mayrhofer, H. Euchner, Electron-configuration stabilized (W,Al)B₂ solid solutions, *Acta Materialia* 174 (2019) 398–405. doi:10.1016/j.actamat.2019.05.056.
- [27] J. Haines, J. M. Léger, G. Bocquillon, SYNTHESIS AND DESIGN OF SUPERHARD MATERIALS, *Annual Review of Materials Research* 31 (2001). doi:10.1146/annurev.matsci.31.1.1.
- [28] Z. W. Ji, C. H. Hu, D. H. Wang, Y. Zhong, J. Yang, W. Q. Zhang, H. Y. Zhou, Mechanical properties and chemical bonding of the Os-B system: A first-principles study, *Acta Materialia* 60 (10) (2012) 4208–4217. doi:10.1016/j.actamat.2012.04.015.
- [29] H. O. Pierson, A. W. Mullendore, Thick boride coatings by chemical vapor deposition, *Thin Solid Films* 95 (2) (1982) 99–104. doi:10.1016/0040-6090(82)90229-2.
- [30] K. Takagi, High tough boride base cermets produced by reaction sintering, *Materials Chemistry and Physics* 67 (1-3) (2001) 214–219. doi:10.1016/S0254-0584(00)00442-9.
- [31] P. L. Raffo, R. F. Hehemann, GRAIN GROWTH IN DILUTE TUNGSTEN-BORON ALLOYS, Tech. rep., National Aeronautics and Space Administration, Washington, DC (1965).
- [32] R. Telle, G. Petzow, Strengthening and toughening of boride and carbide hard material composites, *Materials Science and Engineering: A* 105-106 (1988) 97–104. doi:10.1016/0025-5416(88)90485-5.
- [33] D. C. Halverson, A. J. Pyzik, I. A. Aksay, W. E. Snowden, Processing of Boron Carbide-Aluminum Composites, *Journal of the American Ceramic Society* 72 (5) (1989) 775–780. doi:10.1111/j.1151-2916.1989.tb06216.x.
- [34] A. Y. Artamonov, Y. K. Lapshov, M. V. Kozachenko, D. Z. Yurchenko, E. M. Dudnik, Physical and technical properties of alloys of the system W - BN, *Soviet Powder Metallurgy and Metal Ceramics* 6 (9) (1967) 727–731. doi:10.1007/BF00773497.
- [35] E. Ivanov, E. del Rio, Preparation of W-W₂B composites from W-BN powders and properties of W-B-N barrier for copper metallization, *International Journal of Refractory Metals and Hard Materials* 72 (2018) 223–227. doi:10.1016/J.IJRMHM.2017.12.007.
- [36] ASTM, Standard Test Methods for Flexural Properties of Unreinforced and Reinforced Plastics and Electrical Insulating Materials, ASTM Standards (2017).
- [37] J. Klaput, Application of Small Punch Test Method in Studies of the 14MoV63 Steel Before and After Revitalisation, *Archives of Metallurgy and Materials* 60 (1) (2015). doi:10.1515/amm-2015-0007.
- [38] E. W. Neuman, G. E. Hilmas, W. G. Fahrenholtz, Strength of Zirconium Diboride to 2300°C, *Journal of the American Ceramic Society* 96 (1) (2013) 47–50. doi:10.1111/jace.12114.
- [39] D. Demirskyi, I. Solodkyi, T. Nishimura, Y. Sakka, O. Vasylykiv, High-temperature strength and plastic deformation behavior of niobium diboride consolidated by spark plasma sintering, *Journal of the American Ceramic Society* 100 (11) (2017) 5295–5305. doi:10.1111/jace.15048.
- [40] D. Kalish, E. V. Clougherty, K. Kreder, Strength, Fracture Mode, and Thermal Stress Resistance of HfB₂ and ZrB₂, *Journal of the American Ceramic Society* 52 (1) (1969) 30–36. doi:10.1111/j.1151-2916.1969.tb12655.x.
- [41] J.-i. Matsushita, T. Suzuki, A. Sano, High Temperature Strength of TiB₂ Ceramics, *Journal of the Ceramic Society of Japan* 101 (1177) (1993) 1074–1077. doi:10.2109/jcersj.101.1074.
- [42] M. de Jong, W. Chen, T. Angsten, A. Jain, R. Notestine, A. Gamst, M. Sluiter, C. Krishna Ande, S. van der Zwaag, J. J. Plata, C. Toher, S. Curtarolo, G. Ceder, K. A. Persson, M. Asta, Charting the complete elastic properties of inorganic crystalline compounds, *Scientific Data* 2 (2015). doi:10.1038/sdata.2015.9.
- [43] T. Palacios, A. Jiménez, A. Muñoz, M. Monge, C. Ballesteros, J. Pastor, Mechanical characterisation of tungsten–1 wt.% yttrium oxide as a function of temperature and atmosphere, *Journal of Nuclear Materials* 454 (1-3) (2014) 455–461. doi:10.1016/J.JNUCMAT.2014.09.012.
- [44] Y. Chen, Y. Wu, F. Yu, J. Chen, Microstructure and mechanical properties of tungsten composites co-strengthened by dispersed TiC and La₂O₃ particles, *International Journal of Refractory Metals and Hard Materials* 26 (6) (2008) 525–529. doi:10.1016/J.IJRMHM.2007.12.004.
- [45] G.-M. Song, Y.-J. Wang, Y. Zhou, The mechanical and thermophysical properties of ZrC/W composites at elevated temperature, *Materials Science and Engineering: A* 334 (1-2) (2002) 223–232. doi:10.1016/S0921-5093(01)01802-0.
- [46] G. M. Song, Y. Zhou, Y. J. Wang, T. C. Lei, Elevated Temperature Strength of a 20 vol % ZrCp/W Composite, *Journal of Materials Science Letters* 17 (20) (1998) 1739–1741. doi:10.1023/A:1006639606300.
- [47] Y. Wang, Q. Yan, Grain boundary strengthened W-ZrB₂ alloy via freeze-drying technique and spark plasma sintering, *Fusion Engineering and Design* 149 (March) (2019) 111333. doi:10.1016/j.fusengdes.2019.111333.
- [48] G. S. Pisarenko, V. A. Borisenko, Y. A. Kashalyan, The effect of temperature on the hardness

- and modulus of elasticity of tungsten and molybdenum (20–2700†), Soviet Powder Metallurgy and Metal Ceramics 1 (5) (1964) 371–374. doi:10.1007/BF00774121.
- [49] G.-M. Song, Y.-J. Wang, Y. Zhou, Thermomechanical properties of TiC particle-reinforced tungsten composites for high temperature applications, International Journal of Refractory Metals and Hard Materials 21 (1-2) (2003) 1–12. doi:10.1016/S0263-4368(02)00105-1.
- [50] I. Wesemann, W. Spielmann, P. Heel, A. Hoffmann, Fracture strength and microstructure of ODS tungsten alloys, International Journal of Refractory Metals and Hard Materials (2010). doi:10.1016/j.ijrmhm.2010.05.009.
- [51] J.-l. Fan, T. Liu, H.-c. Cheng, D.-l. Wang, Preparation of fine grain tungsten heavy alloy with high properties by mechanical alloying and yttrium oxide addition, Journal of Materials Processing Technology 208 (1-3) (2008) 463–469. doi:10.1016/J.JMATPROTEC.2008.01.010.
- [52] R. Liu, Z. Xie, Q. Fang, T. Zhang, X. Wang, T. Hao, C. Liu, Y. Dai, Nanostructured yttria dispersion-strengthened tungsten synthesized by sol-gel method, Journal of Alloys and Compounds 657 (2016) 73–80. doi:10.1016/J.JALLCOM.2015.10.059.
- [53] A. G. Atkins, D. Tabor, Hardness and deformation properties of solids at very high temperatures, Proceedings of the Royal Society of London. Series A. Mathematical and Physical Sciences 292 (1431) (1966) 441–459. doi:10.1098/rspa.1966.0146.
- [54] C. Ren, Z. Fang, M. Koopman, B. Butler, J. Paramore, S. Middlemas, Methods for improving ductility of tungsten - A review, International Journal of Refractory Metals and Hard Materials 75 (2018) 170–183. doi:10.1016/J.IJRMHM.2018.04.012.
- [55] M. Rieth, S. Dudarev, S. Gonzalez de Vicente, J. Aktaa, T. Ahlgren, S. Antusch, D. Armstrong, M. Balden, N. Baluc, M.-F. Barthe, Recent progress in research on tungsten materials for nuclear fusion applications in Europe, Journal of Nuclear Materials 432 (1-3) (2013) 482–500. doi:10.1016/J.JNUCMAT.2012.08.018.
- [56] D. Scheiber, V. I. Razumovskiy, P. Puschnig, R. Pippan, L. Romaner, Ab initio description of segregation and cohesion of grain boundaries in W-25 at.% Re alloys, Acta Materialia 88 (2015) 180–189. doi:10.1016/j.actamat.2014.12.053.
- [57] L. Romaner, C. Ambrosch-Draxl, R. Pippan, Effect of Rhenium on the Dislocation Core Structure in Tungsten, Physical Review Letters 104 (19) (2010) 195503. doi:10.1103/PhysRevLett.104.195503.
- [58] Y.-H. Li, H.-B. Zhou, L. Liang, N. Gao, H. Deng, F. Gao, G. Lu, G.-H. Lu, Transition from ductilizing to hardening in Tungsten: the dependence on Rhenium distribution, Acta Materialia 181 (2019) 110–123. doi:10.1016/j.actamat.2019.09.035.
- [59] J. Reiser, J. Hoffmann, U. Jäntschi, M. Klimenkov, S. Bonk, C. Bonnekoh, M. Rieth, A. Hoffmann, T. Mroczek, Ductilisation of tungsten (W): On the shift of the brittle-to-ductile transition (BDT) to lower temperatures through cold rolling, International Journal of Refractory Metals and Hard Materials (2016). doi:10.1016/j.ijrmhm.2015.09.001.
- [60] J. Reiser, J. Hoffmann, U. Jäntschi, M. Klimenkov, S. Bonk, C. Bonnekoh, A. Hoffmann, T. Mroczek, M. Rieth, Ductilisation of tungsten (W): On the increase of strength AND room-temperature tensile ductility through cold-rolling, International Journal of Refractory Metals and Hard Materials (2017). doi:10.1016/j.ijrmhm.2016.10.018.
- [61] T. Shen, Y. Dai, Y. Lee, Microstructure and tensile properties of tungsten at elevated temperatures, Journal of Nuclear Materials 468 (2016) 348–354. doi:10.1016/J.JNUCMAT.2015.09.057.
- [62] Q. Wei, L. Kecskes, Effect of low-temperature rolling on the tensile behavior of commercially pure tungsten, Materials Science and Engineering: A 491 (1-2) (2008) 62–69. doi:10.1016/J.MSEA.2008.01.013.
- [63] Q. Yan, X. Zhang, T. Wang, C. Yang, C. Ge, Effect of hot working process on the mechanical properties of tungsten materials, Journal of Nuclear Materials 442 (1-3) (2013) S233–S236. doi:10.1016/J.JNUCMAT.2013.01.307.
- [64] Y. Zhang, A. V. Ganeev, J. T. Wang, J. Q. Liu, I. V. Alexandrov, Observations on the ductile-to-brittle transition in ultrafine-grained tungsten of commercial purity, Materials Science and Engineering: A 503 (1-2) (2009) 37–40. doi:10.1016/J.MSEA.2008.07.074.
- [65] T. Hao, Z. Fan, T. Zhang, G. Luo, X. Wang, C. Liu, Q. Fang, Strength and ductility improvement of ultrafine-grained tungsten produced by equal-channel angular pressing, Journal of Nuclear Materials 455 (1-3) (2014) 595–599. doi:10.1016/J.JNUCMAT.2014.08.044.
- [66] C. Ren, Z. Z. Fang, L. Xu, J. P. Ligda, J. D. Paramore, B. G. Butler, An investigation of the microstructure and ductility of annealed cold-rolled tungsten, Acta Materialia 162 (2019) 202–213. doi:10.1016/j.actamat.2018.10.002.
- [67] J. Reiser, M. Rieth, A. Möslang, B. Dafferner, A. Hoffmann, X. Yi, D. Armstrong, Tungsten foil laminate for structural divertor applications – Tensile test properties of tungsten foil, Journal of Nuclear Materials 434 (1-3) (2013) 357–366. doi:10.1016/J.JNUCMAT.2012.12.003.
- [68] V. Krsjak, S. Wei, S. Antusch, Y. Dai, Mechanical properties of tungsten in the transition temperature range, Journal of Nuclear Materials 450 (1-3) (2014) 81–87. doi:10.1016/J.JNUCMAT.2013.11.019.
- [69] J. Habainy, S. Iyengar, Y. Lee, Y. Dai, Fatigue behavior

ior of rolled and forged tungsten at 25°, 280° and 480 °C, Journal of Nuclear Materials 465 (2015) 438–447. doi:10.1016/J.JNUCMAT.2015.06.032.

- [70] X. Zhang, Q. Yan, S. Lang, M. Xia, C. Ge, Texture evolution and basic thermal-mechanical properties of pure tungsten under various rolling reductions, Journal of Nuclear Materials (2016). doi:10.1016/j.jnucmat.2015.04.001.
- [71] M. Rieth, B. Dafferner, Limitations of W and W-1%La₂O₃ for use as structural materials, Journal of Nuclear Materials (2005). doi:10.1016/j.jnucmat.2005.03.013.
- [72] Y. Kitsunai, H. Kurishita, H. Kayano, Y. Hiraoka, T. Igarashi, T. Takida, Microstructure and impact properties of ultra-fine grained tungsten alloys dispersed with TiC, Journal of Nuclear Materials (1999). doi:10.1016/S0022-3115(98)00753-3.